Pipeline for effective denoising of digital mammography and digital breast tomosynthesis

Lucas R. Borges[a,b], Predrag R. Bakic[b], Alessandro Foi[c], Andrew D. A. Maidment[b], and Marcelo A. C. Vieira[a]

[a]Department of Electrical and Computer Engineering, University of São Paulo, São Carlos, Brazil
[b]Department of Radiology, University of Pennsylvania, Philadelphia, United States
[c]Department of Signal Processing, Tampere University of Technology, Tampere, Finland

ABSTRACT

Denoising can be used as a tool to enhance image quality and enforce low radiation doses in X-ray medical imaging. The effectiveness of denoising techniques relies on the validity of the underlying noise model. In full-field digital mammography (FFDM) and digital breast tomosynthesis (DBT), calibration steps like the detector offset and flat-fielding can affect some assumptions made by most denoising techniques. Furthermore, quantum noise found in X-ray images is signal-dependent and can only be treated by specific filters. In this work we propose a pipeline for FFDM and DBT image denoising that considers the calibration steps and simplifies the modeling of the noise statistics through variance-stabilizing transformations (VST). The performance of a state-of-the-art denoising method was tested with and without the proposed pipeline. To evaluate the method, objective metrics such as the normalized root mean square error (N-RMSE), noise power spectrum, modulation transfer function (MTF) and the frequency signal-to-noise ratio (SNR) were analyzed. Preliminary tests show that the pipeline improves denoising. When the pipeline is not used, bright pixels of the denoised image are under-filtered and dark pixels are over-smoothed due to the assumption of a signal-independent Gaussian model. The pipeline improved denoising up to 20% in terms of spatial N-RMSE and up to 15% in terms of frequency SNR. Besides improving the denoising, the pipeline does not increase signal smoothing significantly, as shown by the MTF. Thus, the proposed pipeline can be used with state-of-the-art denoising techniques to improve the quality of DBT and FFDM images.

Keywords: Variance stabilization, denoising, full field digital mammography, digital breast tomosynthesis

1. INTRODUCTION

Full-field digital mammography (FFDM) and digital breast tomosynthesis (DBT) are the most common imaging modalities used for breast cancer screening programs. In breast cancer screening programs, asymptomatic women are exposed to low doses of X-ray radiation. Thus, to guarantee the safety of the patients, the International Basic Safety Standards for Protection against Ionizing Radiation and for the Safety of Radiation Sources instructs that radiation exposures must "…be the minimum necessary to achieve the required diagnostic objective…" [1]. To improve image quality and maintain low radiation levels, a number of authors have investigated the advantages and limitations of applying denoising algorithms to FFDM and DBT images [2] [3] [4]. The common hypothesis of these works is that denoising can improve cancer detection by suppressing the image noise.

The effectiveness of denoising algorithms relies on the correct modeling of the noise statistics. Specifically, the noise found in FFDM and DBT images can be described by a Gaussian-Poisson model. The Gaussian portion describes additive fluctuations of the pixel value which can be caused by, *e.g.*, electronic and thermal noise. The Poisson model accounts for quantum noise, which is inherent to the process of photon generation and detection.

To facilitate the process of noise modeling, a common approach is to use raw images as input for the denoising methods. Although the raw images are the crudest data reported by clinical equipment, some post-processing steps related to detector calibration are incorporated; these must be considered during the denoising process. For example, properties such as the inverse square law and heel effect negatively affect the uniformity of the field, and are frequently compensated by changes in the detector gain (flat-field correction) [5]. Another example of calibration is the pixel offset. The offset is applied to ensure the non-negativity of the pixels. This offset affects the linearity between entrance dose and overall pixel signal.

Medical Imaging 2017: Physics of Medical Imaging, edited by Thomas G. Flohr, Joseph Y. Lo, Taly Gilat Schmidt, Proc. of SPIE Vol. 10132, 1013206 · © 2017 SPIE
CCC code: 1605-7422/17/$18 · doi: 10.1117/12.2255058

Additionally, quantum noise is signal-dependent. Many of the best denoising methods in the literature are designed assuming signal-independent Gaussian noise [6] [7]. Mathematical tools such as variance-stabilizing transformations (VST) are capable of eliminating the dependency between noise and signal. If properly applied, these are powerful tools that may be used for denoising FFDM and DBT images.

Therefore, it is essential to prepare the data correctly and choose appropriate tools before denoising FFDM and DBT images. In this work, we propose a pipeline for FFDM and DBT denoising that considers the calibration steps and allows easy modeling of the noise statistics through variance stabilization transformations. Using the proposed pipeline, it is possible to successfully process FFDM and DBT images using any denoising technique designed for Gaussian signal-independent noise.

2. NOISE MODEL & PROBLEM DEFINITION

Consider $z^o(i,j)$ as pixels from a raw ("for processing") FFDM image or from a raw DBT projection, where (i,j) are spatial coordinates. We model $z^o(i,j)$ as

$$z^o(i,j) = \alpha(i,j)\mathcal{P}\big(y(i,j)\big) + \sigma_E\eta \ + \tau\,, \tag{1}$$

where $\alpha(i,j)$ are spatially varying detector gain, $\mathcal{P}\big(y(i,j)\big)$ indicates a Poisson-distributed variate with parameter $y(i,j)$, $y(i,j)$ is the underlying noise-free signal, σ_E is the standard deviation of the electronic noise, η is signal-independent random noise with zero mean and unit variance and τ is the constant signal offset. The conditional expectation and variance of $z^o(i,j)$ given $y(i,j)$ are:

$$E\{z^o(i,j)|y(i,j)\} = \alpha(i,j)y(i,j) + \tau, \qquad var\{z^o(i,j)|y(i,j)\} = \alpha^2(i,j)y(i,j) + \sigma_E^2, \tag{2}$$

The detector gain $\alpha(i,j)$ and the detector offset τ describe the quantum gain and the modifications on the signal due to the calibration steps that are performed prior to the storage of the raw DICOM file. The quantum gain results from the uncertainties related to x-ray generation, transmission and detection; and the calibration is responsible for the correction of non-uniformities caused by properties such as the heel effect, inverse square law, and dark currents (flat-fielding).

Note that the variance of z^o depends on the electronic noise $\sigma_E\eta$ and also on the underlying signal $y(i,j)$ and detector gain $\alpha(i,j)$, which are spatially dependent. The goal of this work is to obtain an estimate $\hat{z}^o(i,j)$ of the noiseless calibrated signal using the raw data $z^o(i,j)$.

3. MATERIALS & METHODS

Many state-of-the-art denoising algorithms assume input signals contaminated with signal-independent Gaussian noise. This assumption limits the choice of denoising filters that can effectively be applied to FFDM and DBT images. To overcome this issue, we use variance-stabilizing transformations (VST) to convert a signal-dependent variable into an approximately Gaussian signal-independent variable, thereby increasing the number of filtering algorithms that can be used. One well-known VST for Poisson-Gaussian variables is the generalized Anscombe transformation (GAT) [8]. However, to correctly stabilize the noise, the calibration parameters $\alpha(i,j)$ and τ must be estimated and removed from $z^o(i,j)$ prior to the application of the VST.

Thus, before denoising the raw data we propose to use a pipeline with two preliminary steps: calibration removal and variance stabilization. In the former step, the image is linearized and the quantum gain is removed. The latter step consists of choosing an appropriate variance stabilization transform that converts a mixture of Gaussian-Poisson distributions into a signal-independent Gaussian distribution. It is important to emphasize that the appropriate inverse transform must be applied after denoising, and the image must be recalibrated. Figure 1 presents an overview of the proposed pipeline.

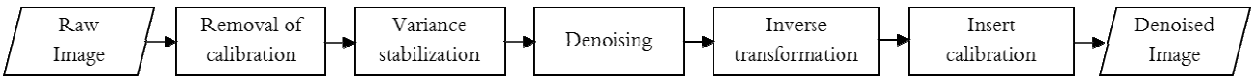

Figure 1. Overall schematic of the proposed pipeline.

3.1. Calibration removal

The goal of this section is to estimate the uncalibrated signal from the available raw image $z^o(i,j)$. Trivially, we can define the uncalibrated signal as:

$$S(i,j) = \frac{z^o(i,j) - \tau}{\alpha(i,j)}. \tag{3}$$

Therefore, to obtain the uncalibrated noisy signal $S(i,j)$ it is necessary to estimate the pixel offset τ and the pixel gain $\alpha(i,j)$. The constant τ can be estimated in various ways. We adopted the method defined by the National Health Service Breast Screening Programme (NHSBSP) [9]. An alternative method for calculating τ consists of acquiring dark-field images.

Next, we estimate the detector gain $\alpha(i,j)$. The best way to obtain $\alpha(i,j)$ would be by accessing the calibration data of the clinical system. However, this information is not always available and thus has to be estimated from acquired images. To this end, we first express the underlying signal $y(i,j)$ as a function of the expectation of $z^o(i,j)$, starting from equation (2):

$$y(i,j) = \frac{E\{z^o(i,j)|y(i,j)\} - \tau}{\alpha(i,j)}. \tag{4}$$

Then, substituting equation (4) into the variance defined in equation (2), we obtain:

$$\alpha(i,j) = \frac{var\{z^o(i,j)|y(i,j)\} - \sigma_E^2}{E\{z^o(i,j)|y(i,j)\} - \tau}. \tag{5}$$

The variance σ_E^2 of the signal-dependent noise can be estimated using tools described in the literature [10], as explained in the results section. The total noise variance of the calibrated signal $var\{z^o(i,j)|y(i,j)\}$ and the expectation of the calibrated signal $E\{z^o(i,j)|y(i,j)\}$ can both be estimated from uniform calibration images. Therefore, a good approximation of $\alpha(i,j)$ can be found using equation (5). Finally, $S(i,j)$ can be estimated using the relation defined by equation (3).

3.2. Variance-stabilizing transformation (VST)

Variance-stabilizing transformations are mathematical tools capable of converting signal-dependent noise distributions into signal-independent noise with an approximately Gaussian shape and constant variance. For Poisson-Gaussian data, a common transformation is the generalized Anscombe transformation (GAT), defined by [8]. For observations such as the uncalibrated signal $S(i,j)$, the GAT is defined as

$$\mathcal{A}\big(S(i,j)\big) = 2\sqrt{S(i,j) + \frac{3}{8} + \sigma_E^2}\,, \tag{6}$$

where $\mathcal{A}\big(S(i,j)\big)$ is the stabilized signal, which can be modeled as corrupted exclusively by standard Gaussian noise, $\mathcal{N}(0,1)$. Denoising can finally be applied to the signal, and the denoised image can be recovered by applying the appropriate inverse transformation. The image is then recalibrated by multiplying the signal by the estimated $\alpha(i,j)$ matrix and adding τ.

3.3. Denoising

After stabilization of the variance, we treat the noise as additive independent Gaussian white noise with known variance. In particular, in the case of the generalized Anscombe VST, the variance is unitary. Many denoising methods are suitable for this standard type of noise degradation. A review of the most significant approaches can be found, e.g., in [11] [12]. For the purpose of the present work, we utilize the popular BM3D denoising algorithm [7]. This highly competitive algorithm synergistically combines three important elements found in many modern image filters:

A) The use of patch-based estimates, i.e. a redundant image representation composed of multiple overlapping small patches or blocks;

B) The use of nonlocal self-similarity as a regularization prior, i.e. leveraging the fact that natural images contain a large number of mutually similar patches at different locations and that noise can be attenuated by adaptively enforcing the mutual similarity between patches;

C) Transform-domain sparsity, i.e. the fact that natural signals enjoy a compact representation with respect to suitable decorrelating transforms (e.g., discrete cosine or wavelets) where most of the energy is concentrated in few large-magnitude coefficients within the transform spectrum, and where regularization can be effectively implemented by shrinkage (e.g., hard thresholding) of the spectrum.

Specifically, BM3D represents the image through a collection of spectra of all groups of mutually similar patches by stacking the mutually similar image blocks into 3D data arrays, and by applying a 3-D decorrelating transform to these groups, BM3D achieves an enhanced sparse and redundant representation of the image. The inverse 3D transformation of a shrunk group spectrum yields a group of jointly filtered image patches. Each pixel in the image is then estimated by a multitude of filtered patches, which are finally combined via an adaptive averaging procedure (so-called aggregation) to yield the final image estimate.

3.4. Inverse VST

The denoised image d, obtained after variance stabilization, has to undergo an inverse VST transformation to match the range of S. For this task, we use the exact unbiased inverse of the generalized Anscombe transform $\mathcal{A}_{EUI}^{-1}$, as proposed in [13]:

$$\mathcal{A}_{EUI}^{-1}(d) = \frac{1}{4}d^2 + \frac{1}{4}\sqrt{\frac{3}{2}}d^{-1} - \frac{11}{8}d^{-2} + \frac{5}{8}\sqrt{\frac{3}{2}}d^{-3} - \frac{1}{8} - \sigma_E^2 \tag{7}$$

The need for this particular inverse stems from the fact that the forward VST is necessarily a nonlinear mapping, which thus does not commute with the mathematical expectation: $E\{\mathcal{A}(S)|y\} = \mathcal{A}(E\{S|y\})$. The inverse [13] is specially designed so that $\mathcal{A}_{EUI}^{-1}(E\{\mathcal{A}(S)|y) = E\{S|y\}$, exactly, and for any y. Therefore, applying $\mathcal{A}_{EUI}^{-1}$ to the output of BM3D is justified as soon as we consider that, formally, denoising of $\mathcal{A}(S)$ aims to approximate the conditional expectation $d \approx E\{\mathcal{A}(S)|y\}$. We refer the reader to [13] for more details on the optimal statistical properties of $\mathcal{A}_{EUI}^{-1}$.

3.5. Metrics

To assess the performance of the proposed pipeline, objective metrics were calculated before denoising, after denoising without the proposed pipeline, and after denoising with the proposed pipeline. The normalized root mean square error (N-RMSE) was used to evaluate the performance of the method in the spatial domain. We adopted the root mean square error normalized by the signal standard deviation:

$$NRMSE(a,r) = \frac{1}{\sigma_{gt}}\sqrt{\frac{1}{MN}\sum_{i=1}^{M}\sum_{j=1}^{N}\big(a(i,j) - r(i,j)\big)^2}\,, \tag{8}$$

where σ_{gt} is the standard deviation of the signal, $r(i,j)$ are pixels from a reference noiseless image, $a(i,j)$ are the pixels from the image being evaluated, M and N are image dimensions. As our noise model is signal-dependent, we present the improvements in the N-RMSE as a function of the gray level.

The second objective metric used was the normalized power spectrum of the residual noise (NNPS) [5], which evaluates the noise in terms of frequency components. The NNPS is widely used as a quality metric. We also analyzed the signal smoothing caused by the denoising method. For this purpose, we compare the modulation transfer function (MTF) [5] estimated from the denoised images.

Lastly, we estimated the efficiency of the denoising pipeline in terms of the signal-to-noise ratio as a function of spatial frequency. We define the frequency SNR as:

$$SNR_{dB}(u) = 10\log_{10}\left(\frac{MTF^2(u)}{NNPS(u)}\right), \tag{9}$$

where u are frequency components. The results show the relative improvement in SNR.

3.6. Images

To assess the performance of the proposed pipeline, sets of FFDM and DBT images were acquired using a clinical imaging system Selenia Dimensions (Hologic, Bedford, MA) at the Hospital of the University of Pennsylvania. We chose to perform all tests using a 3D anthropomorphic breast phantom [14] [15]. The phantom allows the acquisition of several instances, facilitating the estimation of the noiseless signal necessary to calculate some of the objective metrics.

The anthropomorphic phantom was prototyped by CIRS, Inc. (Reston, VA) under license of the University of Pennsylvania. It consists of six slabs, each containing simulated anatomical structures manufactured using tissue mimicking materials, based upon a realization of the companion breast software phantom [16]. The phantom simulates a 450 ml breast, compressed to 5 cm, with 17% volumetric breast density (excluding the skin). In addition to the normal breast anatomy, individual pieces of calcium oxalate (99%, Alfa Aesar, Ward Hill, MA), with different sizes were placed between slabs of the phantom to mimic a cluster of microcalcifications. Figure 2 shows a photograph of all the slabs of the anthropomorphic breast phantom used in this study, an example of a FFDM acquisition, and the central slice of a DBT reconstructed image.

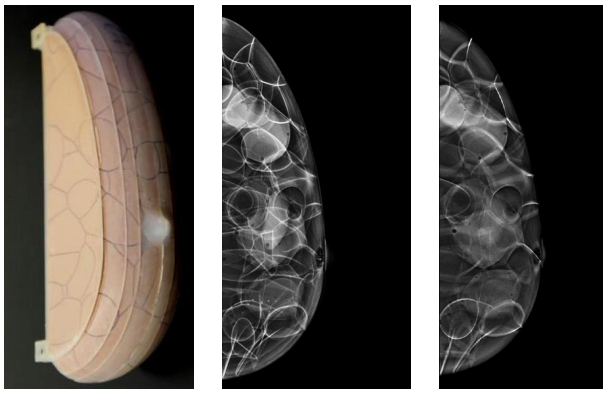

(a) Photograph (b) FFDM (c) DBT

Figure 2. Anthropomorphic phantom used for validation.

First, one FFDM of the phantom was acquired using the automatic exposure control mode (AEC). This exposure was used to define the optimal acquisition settings for the phantom composition (29 kVp, 160 mAs). Next, the acquisition was switched to manual mode and 15 images were acquired using the exposure settings given by the AEC. The current-time product (mAs) was then decreased from the AEC value (160 mAs) to 120 mAs and 80 mAs to simulate lower radiation levels. Five images were acquired at each dose.

Sets of DBT images were also acquired using the same equipment. Again, one exposure was performed to define the optimal exposure parameters, followed by the manual acquisition of 15 sets of DBT projections at the configuration given by the AEC (31 kVp/60 mAs), and 5 additional sets of reduced dose images were acquired at 42 mAs and 30 mAs. For both modalities, an approximation of the noiseless image was calculated by averaging ten acquisitions at the highest dose level.

As mentioned in the previous section, the MTF was used as a measurement for evaluation of signal smoothing. The MTF is commonly calculated using a highly attenuating uniform object positioned over a uniform background, which results on a high contrast step used to estimate the MTF. However, the denoising algorithm proposed in this work takes advantage of the self-similarities found in the input image. Thus, denoising such uniform images and calculating the MTF would yield good results, but it would not represent the real performance of the pipeline in a real application. To

simulate the real denoising performance, metal features were inserted between slabs of the anthropomorphic phantom. This configuration results in images with real structured background that forces the pipeline to perform a challenging denoising task, but at the same time allows the estimation of the MTF using the border of the metal feature. Figure 3 shows ROIs containing the metal inserts used to estimate the MTF.

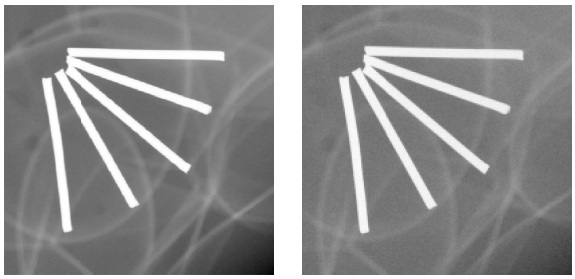

(a) FFDM raw image (b) DBT raw projection

Figure 3. Metal inserts used to calculate the MTF.

The estimation of the calibration parameters requires a set of uniform images acquired with the same equipment as used for the acquisition of the FFDM and DBT input images. For this purpose, we created a pool of uniform images using a 45 mm poly methyl methacrylate (PMMA) block, commonly used for flat-fielding the system. Uniform FFDM images were acquired at the following entrance air kerma: 5.86 mGy, 5.14 mGy, 4.41 mGy and 2.93 mGy. Also, uniform DBT projections were acquired at entrance air kerma of 5.46 mGy, 4.65 mGy, 3.83 mGy and 2.74 mGy.

4. RESULTS & DISCUSSION

4.1 Estimation of detector offset τ

The NHSBSP method [9], which we adopt to estimate the detector offset, consists of acquiring a set of uniform images at a range of current-time products and calculating the mean pixel value (MPV) inside a 100 mm square ROI positioned at the midline, 60 mm from the chest wall. The relation between the detector entrance surface air kerma and MPV is fitted to an affine function, and the MPV at zero air kerma is the estimated τ. Details can be found in [9]. The estimated τ_{FFDM} was 42, and τ_{DBT} was 58.

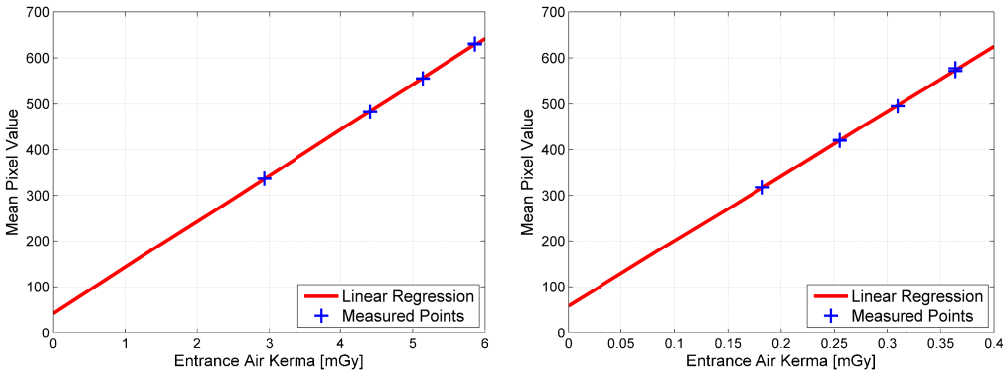

(a) Estimation of τ_{FFDM} (b) Estimation of τ_{DBT}

Figure 4. Linear regressions used to estimate the pixel offset.

4.2. Estimation of electronic noise σ_E^2 and detector gain $\alpha(i,j)$

As defined by equation (5), an initial estimation of σ_E^2 is required to estimate the detector gain $\alpha(i,j)$. For this purpose, we use software [10] available for download at the authors' website [17]. The program can estimate the standard deviation of the additive portion of a Gaussian-Poisson mixture provided that the pixel gain $\alpha(i,j)$ is constant through the field. To meet this requirement, we selected a rectangular ROI with a short span along the chest-nipple direction

(14 mm) and a much longer span along the orthogonal direction (140 mm). Using this elongated layout, we take advantage of the fact that the pixel gain varies more slowly on the orthogonal direction than in the chest-nipple direction. The ROI was taken from 15 realizations of the high dose images after the subtraction of τ. For DBT images, the estimation was performed on the 15 central projections, perpendicular to the field.

The estimated σ_E^2 was 1.8 ± 0.4 for FFDM images, and 7.2 ± 1.3 for DBT images. Note that the variance of the electronic noise estimated from the DBT projection is four times the variance estimated from the FFDM image. This relationship is consistent with the theory, as the DBT system used in this work uses the same detector as used for FFDM, but it performs 2 × 2 pixel binning. Therefore, DBT images are expected to report electronic noise four times higher.

The pixel gain was estimated via equation (5) using the uniform images acquired with the AEC mode. Figure 5 shows the estimated $\alpha(i,j)$ for each spatial position. Note that, as mentioned before, $\alpha(i,j)$ has more relevant changes in the chest wall to nipple direction, than in the orthogonal direction.

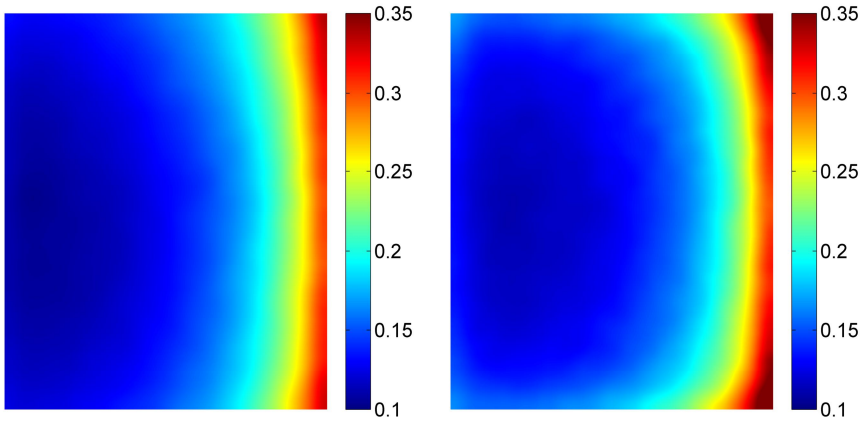

(a) FFDM (b) DBT

Figure 5. Spatially dependent detector gain $\alpha(i,j)$.

4.3. Variance Stabilization

After the calibration was removed following the previous steps, it is possible to stabilize the noise variance using the VST defined by (6). Figure 6 visualizes the local standard deviation calculated using a ROI positioned inside the breast with the AEC acquisition. Note that before stabilization the standard deviation spans a wide range, and is signal dependent as noticed by the presence of structures inherent in the images. Figures 6 (b) and (d) show that the signal-dependency is removed after the VST is applied. Note that, not only the noise is stabilized, but also that the standard deviation is unity. The average of the standard deviation shown in Figure 6 (b) is 1.01, and in Figure 6 (d) is 1.07. Furthermore, we would like to emphasize that the signal-dependency of the noise is much more evident on FFDM images, although it can also be noticed in the DBT image. This shows that the signal-independent electronic noise has higher relative strength on DBT images compared to FFDM. This can be explained by the 2 × 2 binning performed by the DBT system, and by the fact that DBT images have lower overall signal due to the lower radiation used at each projection.

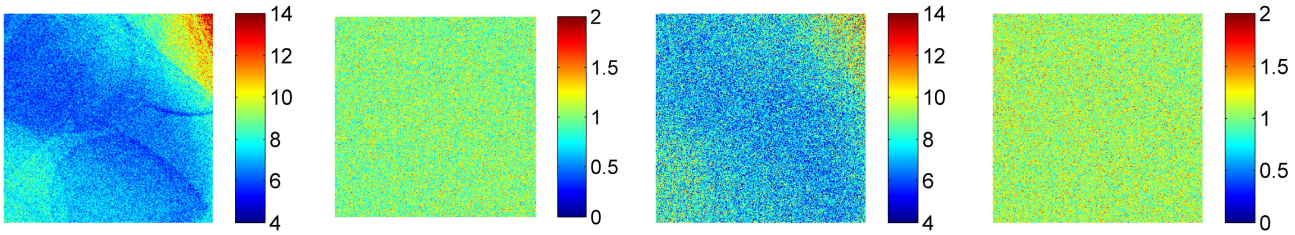

(a) Before VST (FFDM) (b) After VST (FFDM) (c) Before VST (DBT) (d) After VST (DBT)

Figure 6. Standard deviation of FFDM and DBT images before (a,c), and after (b,d) variance stabilization.

4.4. Denoising

Figure 7 shows a magnified portion of the ROI taken from FFDM and DBT images acquired with the AEC configuration, for visual comparison. Figure 7 also shows the pixel profile taken from the region indicated by the lines.

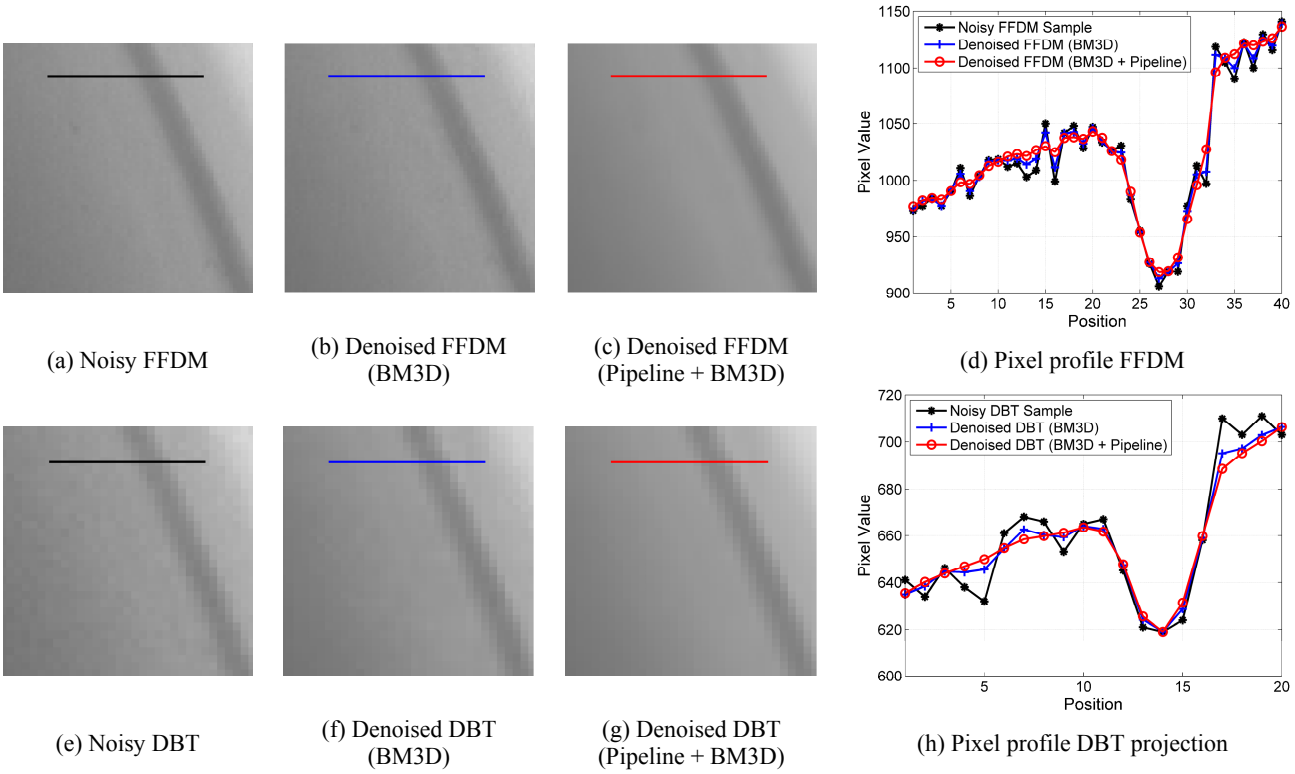

(a) Noisy FFDM (b) Denoised FFDM (BM3D) (c) Denoised FFDM (Pipeline + BM3D) (d) Pixel profile FFDM

(e) Noisy DBT (f) Denoised DBT (BM3D) (g) Denoised DBT (Pipeline + BM3D) (h) Pixel profile DBT projection

Figure 7. Magnified view of a bright area from FFDM and DBT images, and the pixel profile of the region indicated by the line.

As shown by Figure 7, the pipeline improved the denoising process enough to be appreciated visually, and on the line profiles. Figure 8 shows the standard deviation of the residual noise after denoising is performed with and without the pipeline for each pixel. The results show that the proposed pipeline improves the denoising in regions with bright pixels. As the noise is signal-dependent, dark regions are over-smoothed and bright pixels are under-filtered, due to the assumption of signal-independent noise. The DBT results were calculated from the central projection.

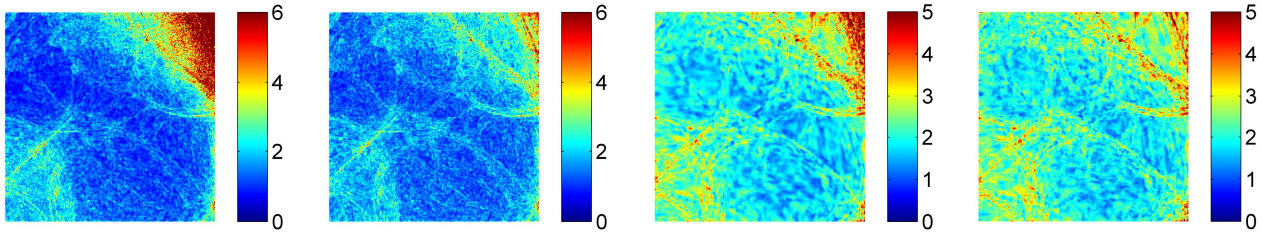

(a) BM3D (FFDM) (b) BM3D + Pipeline (FFDM) (c) BM3D (DBT) (d) BM3D + Pipeline (DBT)

Figure 8. Standard deviation of the residual noise after denoising is performed.

Visual comparison between Figures 6 and 8, with special attention to the color scale, makes evident the potential of the denoising technique chosen in this work. Even with an incorrect noise model, the filter was capable of suppressing a large portion of the noise when the pipeline is not used. However, bright areas such as the top-right corner have higher residual noise when the pipeline is not used.

Since the denoising strength depends on the mean pixel value, in Figure 9 we present the relative improvement on N-RMSE as a function of underlying gray level. Again, results show that bright pixels were not filtered effectively when the pipeline is not applied. The use of the variance-stabilizing transformation improved denoising in those areas.

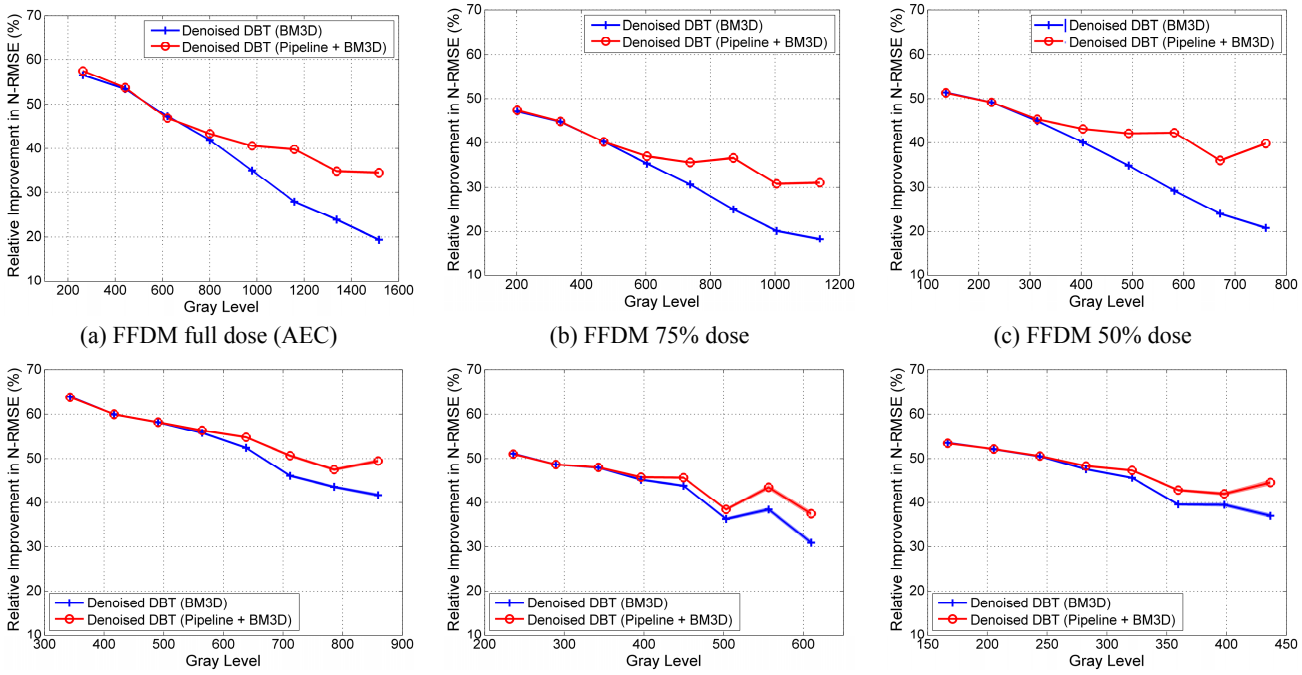

(a) FFDM full dose (AEC) (b) FFDM 75% dose (c) FFDM 50% dose

(d) DBT full dose (AEC) (e) DBT 70% dose (f) DBT 50% dose

Figure 9. N-RMSE and relative improvement in N-RMSE of each method at different entrance dose levels.

Next, the normalized noise power spectrum of the residual noise was calculated, Figure 10 shows the results. Note that the denoising successfully suppressed the noise components especially at high frequencies.

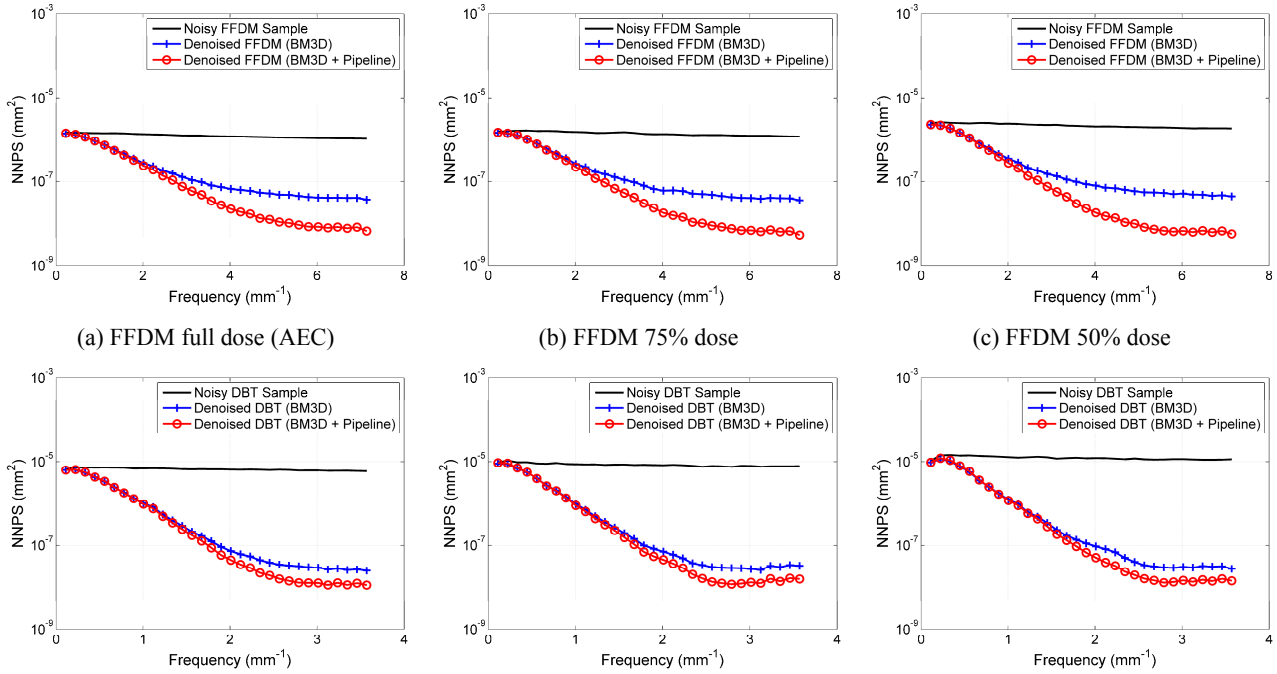

(a) FFDM full dose (AEC) (b) FFDM 75% dose (c) FFDM 50% dose

(d) DBT full dose (AEC) (e) DBT 70% dose (f) DBT 50% dose

Figure 10. Normalized power spectrum of the residual noise from denoised images at different dose levels.

In general, the denoising process consists of a compromise between noise removal and signal smoothing. Therefore, Figure 11 presents the MTF calculated from denoised images. The MTF was calculated using the anthropomorphic phantom with inserted metal features, which generates high contrast borders.

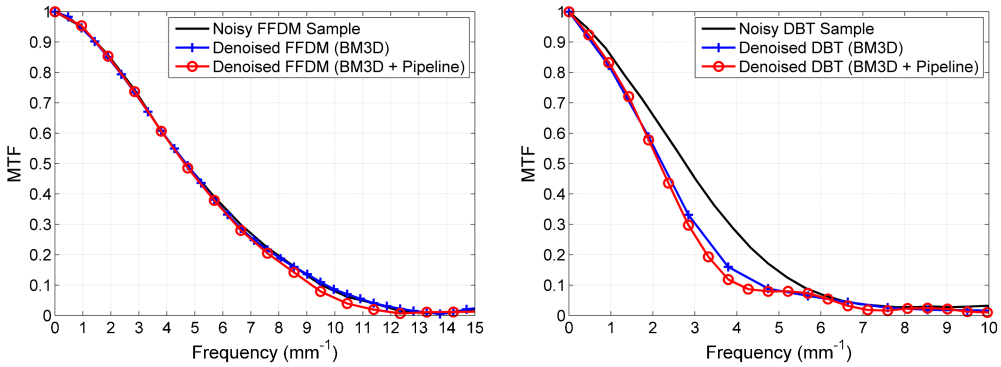

(a) FFDM full dose (AEC) (b) DBT full dose (AEC)

Figure 11. Modulation transfer function of the noisy and denoised images acquired with the AEC mode.

Note that, even though the noise was successfully suppressed in FFDM images, the MTF is preserved. The pipeline improved the denoising in comparison to the BM3D alone with no changes to the MTF. The denoising of DBT images caused a slight drop of the MTF. As DBT projections are acquired at lower radiation levels, they require more aggressive denoising compared to FFDM images, which may justify the slight drop in the MTF.

Lastly, Figure 12 shows the relative improvement of the SNR at the frequency domain. This measurement represents the tradeoff between signal blur and noise suppression.

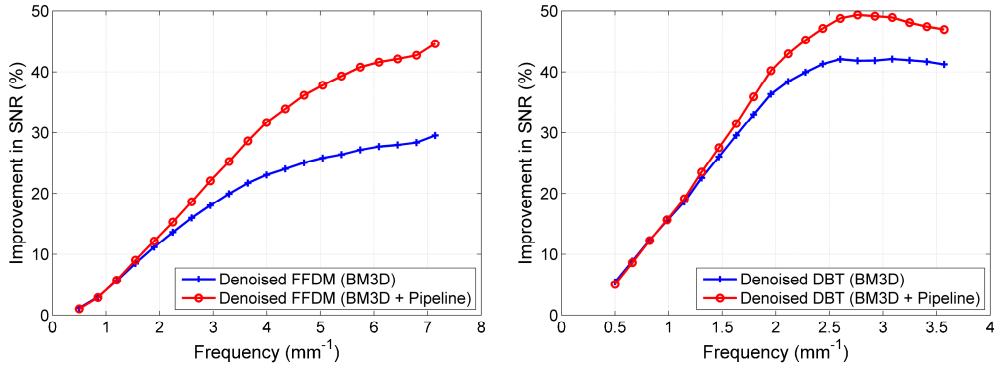

(a) SNR FFDM full dose (AEC) (a) SNR DBT full dose (AEC)

Figure 12. Signal-to-noise ratio as a function of spatial frequency.

Figure 12 shows that the pipeline improves the efficiency of the denoising algorithm. Note that the denoising method is more efficient at suppressing the mid and high frequency noise.

5. CONCLUSION

In this work we investigated the feasibility of a pre-processing pipeline for image denoising. The pipeline is compatible with any denoising technique that assumes additive Gaussian noise. The results support the application of the pipeline, which is especially valuable for FFDM images. Denoising was performed more effectively with the pipeline, showing no relevant detriment to the signal sharpness, as indicated by the MTF. Thus, the efficiency of the denoising was improved, as shown by the relation between signal blur and noise suppression.

ACKNOWLEDGEMENT

This work was supported by the São Paulo Research Foundation (FAPESP), by the Brazilian Foundation for the Coordination of Improvement of Higher Education Personnel (CAPES grant no. 88881.030443/2013-01) and by the Academy of Finland (project no. 252547).

REFERENCES

[1] International Atomic Energy Agency, "Appendix II: Medical exposure," in *International Basic Safety Standards for Protection against Ionizing Radiation and for the Safety of Radiation Sources*. IAEA, pp. 45-56, 1996.

[2] L. C. Romualdo, M. A. Vieira, H. Schiabel, N. D. Mascarenhas and L. R. Borges, "Mammographic image denoising and enhancement using the Anscombe transformation," *Journal of Digital Imaging,* vol. 26, no. 2, pp. 183-197, 2013.

[3] A. Jain, S. Singh and V. Bhateja, "A robust approach for denoising and enhancement of mammographic images contaminated with high density impulse noise," *Int. Journal of Convergence Computing,* vol. 1, no. 1, pp. 38-49, 2013.

[4] G. Wu, J. G. Mainprize and M. Yaffe, "Dose reduction for digital breast tomosynthesis by patch-based denoising in reconstruction," in *Proceedings of the International Workship on Digital Mammography (IWDM)*, Springer, pp. 21-28, 2012.

[5] M. Yaffe, "Digital Mammography," in *Handbook of Medical Imaging: Volume 1 Physics and Psychophysics*, Bellingham, SPIE, pp. 329-372, 2000.

[6] A. Buades, B. Coll and J. Morel, "A Review of Image Denoising Algorithms, with a New One," *Multiscale Model. Simul.,* vol. 4, no. 2, pp. 490-530, 2005.

[7] K. Dabov, A. Foi, V. Katkovnik and K. Egiazarian, "Image Denoising by Sparse 3-D Transform-Domain Collaborative Filtering," *IEEE Trans. Image Process.,* vol. 16, no. 8, pp. 2080-2095, 2007.

[8] B. Zhang, M. J. Fadili, J. -L. Starck and J. -C. Olivo-Marin, "Multiscale Variance-Stabilizing Transform for Mixed-Poisson-Gaussian Processes and its Applications in Bioimaging," in *IEEE International Conference on Image Processing*, San Antonio, 2007.

[9] National Health Service Breast Screening Program, "Calculation of quantitative image quality parameters NHSBSP," NHSBSP Publications, Sheffield, 2009.

[10] A. Foi, M. Trimeche, V. Katkovnik and K. Egiazarian, "Practical Poissonian-Gaussian noise modeling and fitting for single-image raw-data," *IEEE Transactions on Image Processing,* vol. 17, no. 10, pp. 1737-1754, 2007.

[11] V. Katkovnik, A. Foi, K. Egiazarian and J. Astola. "From local kernel to nonlocal multiple-model image denoising," *Int. J. Comput. Vision*, vol. 86, no. 1, pp. 1-32, 2010.

[12] P. Milanfar. "A tour of modern image filtering: New insights and methods, both practical and theoretical," *IEEE Signal Processing Magazine*, vol. 30, no. 1, pp. 106-128, 2013.

[13] M. Makitalo and A. Foi, "A closed-form approximation of the exact unbiased inverse of the Anscombe transformation," *IEEE Transactions on Image Processing,* vol. 20, no. 9, pp. 2697-2698, 2011.

[14] L. Cockmartin, P. R. Bakic, H. Bosmans, A. D. A. Maidment, H. Gall, M. Zerhouni and N. W. Marshall, "Power spectrum analysis of an anthropomorphic breast phantom compared to patient data in 2D digital mammography and breast tomosynthesis," in *International Workshop on Digital Mammography*, Springer, pp. 423-429, 2014.

[15] A.-K. Carton, P. R. Bakic, C. Ullberg, H. Derand and A. D. A. Maidment, "Development of a 3D anthropomorphic breast phantom," *Medical Physics*, vol. 38, no. 2, pp. 891-896, 2011.

[16] D. D. Pokrajac, A. D. A. Maidment and P. R. Bakic, "Optimized generation of high resolution breast anthropomorphic software phantoms," *Medical Physics*, vol. 39, no. 4, pp. 229-2302, 2012.

[17] A. Foi, "Signal-dependent noise modeling, estimation, and removal for digital imaging sensors," 2016. [Online]. Available: www.cs.tut.fi/~foi/sensornoise.html. [Accessed 18 July 2016].